JGR Planets

RESEARCH ARTICLE
10.1029/2024JE008350

Relationships Between HCl, H_2O, Aerosols, and Temperature in the Martian Atmosphere: 1. Climatological Outlook

K. S. Olsen[1,2], A. A. Fedorova[3], D. M. Kass[4], A. Kleinböhl[4], A. Trokhimovskiy[3], O. I. Korablev[3], F. Montmessin[5], F. Lefèvre[5], L. Baggio[5], J. Alday[2], D. A. Belyaev[3], J. A. Holmes[2], J. P. Mason[2], P. M. Streeter[2], K. Rajendran[2], M. R. Patel[2], A. Patrakeev[3], and A. Shakun[3†]

[1]Department of Physics, University of Oxford, Oxford, UK, [2]School of Physical Sciences, The Open University, Milton Keynes, UK, [3]Space Research Institute (IKI), Moscow, Russia, [4]Jet Propulsion Laboratory (JPL), California Institute of Technology, Pasadena, CA, USA, [5]Laboratoire Atmosphères, Milieux, Observations Spatiales (LATMOS/CNRS), Paris, France

Abstract Detecting trace gases such as hydrogen chloride (HCl) in Mars' atmosphere is among the primary objectives of the ExoMars Trace Gas Orbiter (TGO) mission. Terrestrially, HCl is closely associated with active volcanic activity, so its detection on Mars was expected to point to some form of active magmatism/outgassing. However, after its discovery using the mid-infrared channel of the TGO Atmospheric Chemistry Suite (ACS MIR), a clear seasonality was observed, beginning with a sudden increase in HCl abundance from below detection limits to 1–3 ppbv in both hemispheres coincident with the start of dust activity, followed by very sudden and rapid loss at the southern autumnal equinox. In this study, we have investigated the relationship between HCl and atmospheric dust by making comparisons in the vertical distribution of gases measured with ACS and aerosols measured co-located with the Mars Climate Sounder (MCS). This study includes HCl, water vapor, and ozone measured using ACS MIR, water vapor and temperature measured with the near infrared channel of ACS, and temperature, dust opacity, and water ice opacity measured with MCS. In part 1, we show that dust loading has a strong impact in temperature, which controls the abundance of water ice and water vapor, and that HCl is very closely linked to water activity. In part 2, we investigate the quantitative correlations between each quantity and discuss the possible source and sinks of HCl, their likelihood given the correlations, and any issues arising from them.

Plain Language Summary After four full Martian years in orbit since 2018, the ExoMars Trace Gas Orbiter (TGO) has observed three Martian dusty seasons, which occur when it is spring and summer in the southern hemisphere. The first, starting in summer 2018, featured a global dust storm (GDS) after which we made the first detection of hydrogen chloride (HCl) in the Martian atmosphere using the Atmospheric Chemistry Suite (ACS) instrument. Finding this gas was a priority of ExoMars because its presence may indicate that the planet is volcanically active. Since then, we have observed two more dusty periods without a GDS and observed the reappearance of HCl each time. Here, we present the climatology of HCl in both hemispheres over these three dusty periods (in Mars years 34, 35, and 36) and investigate their relationships with temperature and water vapor measured by ACS, and with airborne dust and water ice measured with the Mars Climate Sounder (MCS) on the Mars Reconnaissance Orbiter (MRO). In this paper, we examine how the vertical structure of each quantity changes over time. We show that there is a close relationship between HCl and H_2O, and that both are controlled by temperature, driven by dust loading.

1. Introduction

Chlorine plays a major role in the Earth's atmosphere, cycling between the biosphere, lithosphere, hydrosphere, and atmosphere. In Earth's troposphere, it is closely related to evaporation of sea water and the acidification of rain. In the stratosphere, which is much more similar to the lower atmosphere of Mars in terms of pressure and density, it is closely related to ozone chemistry, participating in catalytic cycles of ozone loss. Aside from sea-salt aerosols and anthropomorphic emissions in the troposphere, the next largest natural source of HCl in Earth's atmosphere is volcanic emissions, which are highly variable (Graedel & Keene, 1995; Keene et al., 1999). The

†Deceased January 2023.

Key Points:

- Comparison of trace gas abundance and aerosol extinction between Atmospheric Chemistry Suite on ExoMars TGO and Mars Climate Sounder on Mars Reconnaissance Orbiter
- Reveal the seasonal changes in hydrogen chloride on Mars
- Show that dust affects atmospheric temperature, which controls water vapor abundance and ice extinction, and thus impacts HCl abundance

Supporting Information:

Supporting Information may be found in the online version of this article.

Correspondence to:

K. S. Olsen,
Kevin.Olsen@physics.ox.ac.uk

Citation:

Olsen, K. S., Fedorova, A. A., Kass, D. M., Kleinböhl, A., Trokhimovskiy, A., Korablev, O. I., et al. (2024). Relationships between HCl, H_2O, aerosols, and temperature in the Martian atmosphere: 1. Climatological outlook. *Journal of Geophysical Research: Planets*, *129*, e2024JE008350. https://doi.org/10.1029/2024JE008350

Received 21 FEB 2024
Accepted 2 AUG 2024

Author Contributions:

Conceptualization: K. S. Olsen, O. I. Korablev, F. Montmessin
Data curation: K. S. Olsen, A. A. Fedorova, D. M. Kass, A. Kleinböhl, A. Trokhimovskiy, L. Baggio, A. Patrakeev, A. Shakun
Formal analysis: K. S. Olsen, A. A. Fedorova, J. Alday, D. A. Belyaev, J. A. Holmes, J. P. Mason, P. M. Streeter, K. Rajendran
Funding acquisition: K. S. Olsen, D. M. Kass, O. I. Korablev, F. Montmessin, M. R. Patel

Investigation: K. S. Olsen, F. Lefèvre, L. Baggio, D. A. Belyaev, J. A. Holmes, J. P. Mason, P. M. Streeter, K. Rajendran, M. R. Patel
Methodology: K. S. Olsen, F. Lefèvre
Project administration: K. S. Olsen, O. I. Korablev, F. Montmessin, M. R. Patel
Resources: K. S. Olsen, A. Trokhimovskiy, O. I. Korablev, F. Montmessin, L. Baggio, J. Alday, J. P. Mason, P. M. Streeter, K. Rajendran, M. R. Patel, A. Patrakeev, A. Shakun
Software: K. S. Olsen
Supervision: K. S. Olsen, J. P. Mason, M. R. Patel
Validation: K. S. Olsen, A. A. Fedorova, F. Lefèvre, J. Alday, D. A. Belyaev, J. A. Holmes, J. P. Mason, P. M. Streeter, K. Rajendran
Visualization: K. S. Olsen
Writing – original draft: K. S. Olsen
Writing – review & editing: K. S. Olsen, A. A. Fedorova, A. Kleinböhl, A. Trokhimovskiy, F. Lefèvre, L. Baggio, J. Alday, D. A. Belyaev, J. A. Holmes, J. P. Mason, P. M. Streeter, K. Rajendran, M. R. Patel

largest mechanisms for the removal of reactive chlorine species on Earth is deposition with rain and reaction with hydrocarbons, especially methane (CH_4), and ozone (O_3) (von Glasow & Crutzen, 2003; Wang et al., 2019).

The presence of Hydrogen chloride (HCl) in the atmosphere of Mars may be an indicator for active geological processes such as volcanism or magmatic processes (Hartogh et al., 2010; Wong et al., 2003). For this reason, the presence of HCl on Mars was long searched for, setting stringent upper limits of 0.2–0.3 parts per billion by volume (ppbv; Hartogh et al., 2010; Krasnopolsky et al., 1997; Villanueva et al., 2013). HCl was recently discovered in the lower atmosphere of Mars using the mid-infrared channel of the Atmospheric Chemistry Suite (ACS MIR) onboard the ExoMars Trace Gas Orbiter (TGO) (Korablev et al., 2021), accomplishing one of the primary objectives of the TGO mission—to detect novel trace gases that may be diagnostic of active geological, or biological, processes. ACS MIR measurements determined volume mixing ratios (VMRs) an order of magnitude higher than previous detection limits, but with strong seasonal cycles—seasons that were not probed in past observation attempts.

ACS MIR began its nominal science phase in April 2018, at Martian solar longitude (L_s) 163° in Mars year (MY) 34. Seasonal dust activity began shortly after the southern vernal equinox at $L_s = 180°$ and developed into the 2018 global dust storm (GDS) (e.g., Kass et al., 2019; Smith, 2019). Once the GDS subsided, which severely limited the lower reach of ACS MIR solar occultation measurements in the Martian atmosphere, the spectral signature of HCl became prominent in ACS MIR spectra through to the end of the Martian year (Korablev et al., 2021). Outside the Martian dusty season, when Mars approaches aphelion, HCl was only detected twice at high northern latitudes (Olsen, Trokhimovskiy, et al., 2021). Over the following perihelion periods in MYs 35 and 36, when it is spring and summer in the southern hemisphere, HCl reappeared, suggesting that its sources and sinks are strongly associated with the seasonal changes in airborne dust loading, water vapor, and atmospheric temperature.

Here, we present the climatology of Martian HCl from three full Martian dusty seasons. HCl abundances are compared to simultaneous measurements of water vapor, ozone and temperature, and coincident measurements of the opacities of dust and water ice measured by the Mars Climate Sounder (MCS) (McCleese et al., 2007) on the Mars Reconnaissance Orbiter (MRO) (Zurek & Smrekar, 2007). This study is divided into two parts; this manuscript, part 1, details the methods by which trace gas abundances are measured with ACS MIR, how co-located measurements made with ACS NIR and MCS are determined and compared, what the climatological evolution of each quantity is, and how each quantity is related to one another. In part 2 (Olsen et al., 2024b), we present a quantitative comparison between each quantity, investigate their correlations, and discuss the possible sources and sinks of atmospheric chlorine on Mars in the context of our observations.

2. Methods

ACS MIR is a cross-dispersion spectrometer operating in solar occultation geometry on the TGO spacecraft, which orbits Mars with an inclination of 74° and a near-circular orbit of 400 km. Solar occultation opportunities arise twice per 2 hr orbit and the spacecraft pointing is shared between ACS and the solar occultation channel of the NOMAD instrument (Nadir and Occultation for Mars Discovery). Occultation opportunities dedicated to ACS MIR measurements are further divided among the configuration of its cross-dispersion gratings.

The ACS MIR instrument consists of foreoptics, collimating mirrors, a primary echelle grating that provides access to the mid-infrared spectral range, a secondary collimator, a steerable diffraction grating that separates the overlapping diffraction orders, and a detector (Korablev et al., 2018). The angle of the secondary grating determines which diffraction orders are measured, and the total instantaneous spectral range. HCl lines are present from across the diffraction band centered around 2,890 cm^{-1}. These HCl lines are present in secondary grating positions 11 and 12, which cover the spectral ranges 2,678–2,948 cm^{-1} (diffraction orders 160–175) and 2,917–3,235 cm^{-1} (orders 173–192), respectively. Each HCl line features a pair of two isotopologues, with the primary, $H^{35}Cl$, being accompanied by the secondary $H^{37}Cl$. This allows the measurement of their ratio (Liuzzi et al., 2021; Trokhimovskiy et al., 2021). Between the start of the mission and the end of MY 36, ACS MIR has recorded 1,127 occultation sequences with position 11 and 1,167 with position 12.

Spectra are recorded on a two-dimensional detector array over which the *x*-axis corresponds to wavenumber and the *y*-axis corresponds to both the diffraction order and the vertical field-of-view (FoV) of the instrument. The raw data appear as several horizontal brightness stripes, where each stripe is a unique diffraction order, the width of

each stripe represents the instantaneous FOV, and dark regions separating the stripes are due to portions of the optics not illuminated by the solar disk. Examples of raw data frames are given in Trokhimovskiy et al. (2020) and Olsen, Lefèvre, et al. (2021).

In solar occultation mode, a series of observations are made from the surface to above the top of the atmosphere (>250 km) with vertical separations of 1–3 km. For each measurement in the occultation series, we can extract several spectra from the two-dimensional data frames for each diffraction order. There are variations in atmospheric temperature, pressure, and instrument line shape across the vertical FoV of the instrument, so spectra extracted from different areas must be treated differently. We therefore extract spectra from 10 to 12 rows of the FoV across the detector array for each diffraction order, and create sets of spectra (each diffraction order for each altitude) for each of these rows. The FoV covers 3.3–3.5 km and these spectra are separated by 275–290 m. This results in an ensemble of 10–12 distinct solar occultation sequences of spectra for each observed solar occultation opportunity (see Olsen, Trokhimovskiy, et al., 2021, for examples). Each of these sets of spectra is analyzed independently and the weighted means of the retrieved vertical profiles of trace gas volume mixing ratio (VMR) are taken to be the best estimate of the target gas' abundance.

Spectral fitting is performed with the JPL Gas Fitting Software Suite (GGG or GFIT) (Irion et al., 2002; Sen et al., 1996; Wunch et al., 2011), which has been developed for use with ACS MIR (Olsen, Lefèvre, et al., 2021). A forward model is computed using the HITRAN2020 spectroscopic line list (Gordon et al., 2021) and vertical profiles of temperature and pressure measured simultaneously using the near infrared channel (NIR) of ACS (Fedorova et al., 2020, 2023). Where available, broadening parameters for a CO_2-rich atmosphere are used for HCl (Wilzewski et al., 2016) and H_2O/HDO (Devi et al., 2017; Gamache et al., 2016). For occultations where a simultaneous ACS NIR temperature profile was not measured, the temperature and pressure are estimated using the Planetary Climate Model (PCM; Forget et al., 1999; Lefèvre et al., 2021) using dust climatologies for each MY from (Montabone et al., 2015, 2020). ACS NIR always operates when ACS MIR does and data are available through $L_s = 240°$ in MY 36. We do not observe biases in the ACS MIR retrievals from the time periods with and without ACS NIR data, and we do not observe biases between temperature data taken from ACS NIR and the PCM.

Spectral fitting is performed over narrow windows ~7 cm^{-1} wide using the non-linear Levenberg-Marquardt method. Positions and widths of spectral fitting windows are shown in Figure S1 in Supporting Information S1. Spectra from each altitude are fitted independently to determine the number densities along the line-of-sight (slant column). A model atmosphere is created with 1 km thick layers and the optical path that the line-of-sight takes through each layer is calculated. This leads to an inverse problem where the measured vector of slant column number densities will be equal to the matrix of slant paths times the vertical profiles of true gas abundances. The resulting solution to this linear inverse problem is the retrieved VMR vertical profile. It is on the 1 km tangent height grid above the Martian areoid.

Retrievals are performed for each of the sets of extracted spectra across the illuminated FoV. The retrieved vertical profile is the weighted mean of these results, and the uncertainty at each altitude is the standard deviation of the mean. The weights are based on the uncertainties of the individual retrievals, the diagonal elements of the covariance matrices. The vertical resolution of ACS MIR observations is 1–3 km depending on the beta angle. Whether HCl, O_3, or H_2O were detected in the ACS MIR spectra was defined by their VMRs being greater than twice (2σ) their uncertainty across two or more tangent heights. For very small abundances at the limits of the ACS MIR capabilities, we ensure that a trace gas detection was made in multiple diffraction orders and at multiple tangent heights, as demonstrated in Korablev et al. (2021). To avoid false-positive results, data above 30 km where the standard deviation of the results from the 10 rows is greater than 4 ppbv are rejected, as are sparse vertical profiles where the tangent heights at which HCl was detected are not continuous. Observations where HCl only appears above 30 km, that do not have robust, verifiable absorption lines visible between 10 and 20 km, are not considered unambiguous detections either. This is based on a careful examination of the fitted absorption features which do not exceed the noise level.

Sources of error in the retrievals come from the determination of tangent heights (define the pressure and temperature for the observed airmass), the determination of the thermal background and stray light (impacts the relative line depths), the a priori temperature and pressure, the characterization of the instrument line shape, and the spectral noise. Measurement of the HCl VMR is very difficult because it is often close to the level of spectral noise, and it is therefore sensitive to each of these. Care is taken in the retrieval to address each of these sources of

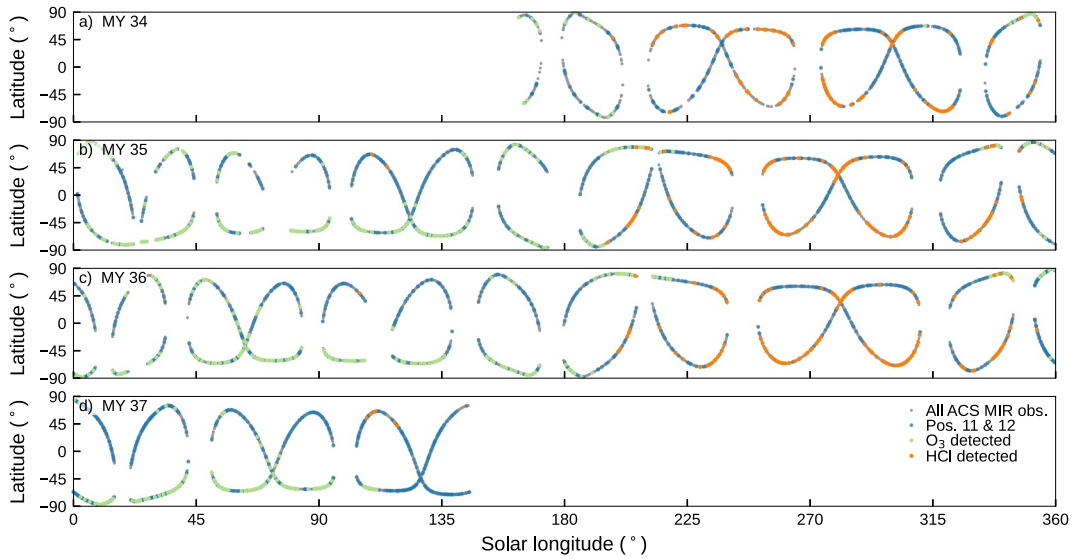

Figure 1. Distribution of ACS MIR solar occultation observations. The data shown are the latitudes of ACS MIR solar occultation observations as a function of time, indicated as solar longitude (L_s) over the year. The panels from top to bottom are for different Mars years (MYs) from the start of ExoMars science operation in MY 34 (a), through MY 37 (d), the current MY at the time of writing. Observations in which ozone was detected are highlighted green, and cover southern fall and winter. Those where HCl was detected are highlighted orange and occur during southern spring and summer.

error, but variability remains between the retrievals from each of the sets of spectra from the detector rows. We are able to validate the retrieval by comparing retrieved water vapor to that from ACS NIR (shown in part 2; Olsen et al., 2024b), and we do not observe biases between ACS NIR and ACS MIR.

This method has proven to be very effective when examining trace gases in the Martian atmosphere whose absorption features approach the noise levels of the signal. The JPL Gas Fitting Software was originally applied to single spectra to measure carbon monoxide (CO), ozone, and HCl (Korablev et al., 2021; Olsen et al., 2020; Olsen, Lefèvre, et al., 2021), and the expansion of the method to use multiple detector rows was developed for HCl (Olsen, Trokhimovskiy, et al., 2021) and then applied to ozone, water vapor, and CO (Alday et al., 2023; Olsen et al., 2022). Example profiles of the VMRs of HCl and H_2O retrieved from the ACS MIR data using these methods are shown in Figure S2 in Supporting Information S1.

3. ACS MIR and MCS Data

The latitudinal distribution of ACS solar occultation observations is shown in Figure 1 from the start of the primary science phase at $L_s = 163°$ in MY 34 to $L_s = 120°$ in MY 37. The latitude of the occultations changes as the orbital plane precesses around Mars and gaps occur when the angle between the Sun and spacecraft's orbital plane (beta) approaches perpendicularity with the Mars-Sun axis. The northern and southern reach is a function of the orbital inclination of Mars and the Martian season. Each solar occultation occurs at the local solar terminator, and so the northernmost or southernmost occultation opportunities occur at the edges of the polar day or polar night. Thus, the ACS occultations have the greatest latitudinal extent at the equinoxes.

Perihelion, the closest approach between Mars and the Sun, occurs at $L_s = 251°$ toward the end of southern spring and just before southern summer, while aphelion occurs at $L_s = 71°$ prior to southern winter. Herein we refer to the first half of the Martian year, from the southern autumnal equinox ($L_s = 0°$) to the vernal equinox ($L_s = 180°$), the aphelion period, and the second half of the year as the perihelion period. This is due to the north-south symmetry in the Martian climate exhibited above 5–10 km (Fedorova et al., 2023).

Indicated in Figure 1 are the locations where HCl or ozone were detected in the ACS MIR observations. Both gases show strong seasonal preference and north-south symmetry which will be discussed in detail in Section 4.

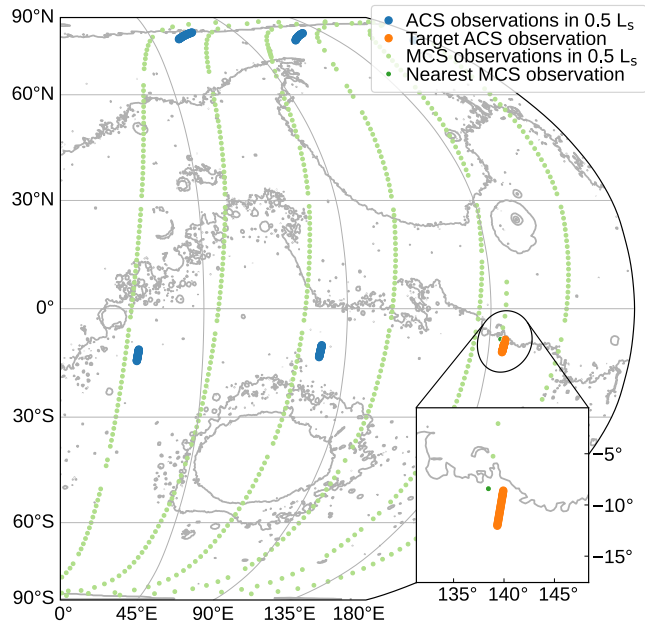

Figure 2. Coincident observations between ACS and MCS. Shown is the eastern hemisphere of Mars with the location of an ACS MIR occultation where HCl was detected and coincident MCS observations were found (orange circles and inset). An area covering 500 km from the occultation tangent point is indicated with a circle. Each MCS observation made within a 0.25° L_s window of the ACS MIR occultation is indicated (green circles), as are other ACS MIR observations (blue circles). For ACS MIR occultation, tangent point from the surface to 50 km are shown as a track. The inset highlights the ACS MIR occultation, the coincident MCS observations, and the MCS observation nearest in space and time to ACS MIR.

MCS is a passive radiometer with nine channels that operates in nadir, off-nadir, and limb geometries. The infrared channels cover absorption features of CO_2, used for retrieval of pressure and temperature, as well as absorption features of aerosols, used for retrieval of water ice and dust opacity along the line-of-sight (McCleese et al., 2007). The dust opacity per km is measured at 21.6 μm and that of water ice is measured at 11.9 μm. The current version of MCS data, v5.2, uses a two-dimensional radiative transfer scheme to correct for lateral gradients in temperatures and aerosols (Kleinböhl et al., 2009, 2017). For a portion of the MCS data set that covers the MY 34 global dust storm, MCS data was reprocessed using a far infrared channel to improve its vertical range (v5.3.2) (Kleinböhl et al., 2020).

The MRO spacecraft is in a Sun-synchronous orbit (inclination 93° at an altitude of 250–316 km. MCS nominally operates in limb viewing mode and makes frequent, 30-s observations throughout its orbit, amassing hundreds of measurements per day over a broad range of latitudes and longitudes. This provides ample opportunity to find coincident measurements between ACS MIR solar occultations, and MCS limb scans. MCS observations at mid-to-low latitudes are made at approximately 03:00 and 15:00 local time, but this time can vary within a ∼2 hr window depending on the time of year, especially at higher latitudes, where the majority of ACS solar occultations occur.

The coincidence criteria set to determine an MCS-ACS coincident measurements was within ±0.125° L_s (∼6 hr) and spatially separated by a distance <500 km. This results in the MCS observation ground track intercepting a solar occultation location for 85% of the ACS observations, often with around ten MCS limb observations per ACS tangent point. An example of the geometry of a coincident measurement is shown in Figure 2, which has all MCS and ACS MIR observations made within the coincidence criteria. Example profiles of the measured quantities compared here, the VMRs or HCl and H_2O measured with ACS MIR, temperatures from ACS NIR and MCS, and the opacities of dust and water ice measured with MCS, are shown in Figures S2 and S3 in Supporting Information S1.

4. Results

4.1. The Climatology of HCl Observed With ACS MIR

Since HCl was observed for the first time in the Martian atmosphere, we have noted that it is apparently correlated with water vapor and behaves with a linked seasonality (Aoki et al., 2021; Korablev et al., 2021; Olsen, Trokhimovskiy, et al., 2021). By the end of 2023, we have made observations of HCl through three perihelion periods in MYs 34, 35, and 36 and have performed retrievals with both positions 11 and 12. This provides an unprecedented opportunity to explore the repeating seasonal changes in HCl over altitude and over time. In general, the VMR of HCl remains below the limits of a definitive detection during the aphelion periods. That is, HCl may be present at low levels, well below 0.5 ppbv, but the absorption features present in such spectra are not prominent beyond the instrument noise, and a low detection limit is determined rather than an HCl VMR (Olsen, Trokhimovskiy, et al., 2021).

Immediately following the southern vernal equinox at $L_s = 180°$, HCl becomes detectable and VMRs increase rapidly. HCl then remains in the Martian atmosphere with VMRs of several ppbv throughout the perihelion period. Around the southern autumnal equinox, the HCl VMR falls off dramatically, and remain low through the next aphelion period until it is spring in the southern hemisphere again. Such an overall trend is apparent in both hemispheres, but the magnitudes in the southern hemisphere grow much larger, and vary in a more dynamic fashion, than in the north.

Figure 3 shows how the vertical distribution of HCl changes with time as observed with ACS MIR over the perihelion periods. There is a strong similarity in the southern hemisphere evolution each MY, and a striking difference between the abundances in the northern and southern hemispheres. It is important to note that the empty space in Figure 3 does not indicate a lack of HCl but no observations. Gray shading indicates when secondary grating positions 11 or 12 were used, but HCl remained below a detection threshold. MY 34 was punctuated by the GDS that strongly impeded our ability to probe the lower atmosphere and resulted in the lack of observations between $L_s = 190°$ and 240°, especially below 30 km. Other visible gaps in the data set are due to unfavorable beta angles, as shown in Figure 1. Sections of the latitude coverage are shown in Figure 1 that correspond to each panel in Figure 3 are reproduced in Figure S4 in Supporting Information S1.

In the northern hemisphere, we observe a low abundance of HCl throughout the 5–50 km altitude range during most of the perihelion period. The time of its appearance is correlated with the start of seasonal dust activity (Section 4.3), which leads to warmer atmospheric temperatures and an expansion of the lower atmosphere, bringing water vapor into this altitude range. VMRs observed are between 0.2 and 1.5 ppbv and remain consistent throughout the perihelion period. In MY 34, following the GDS, we see higher abundances, >2 ppbv, between 35 and 45 km. These appear between $L_s = 210°$–240°, after which the high-altitude layer of elevated HCl VMRs falls to between 25 and 35 km. This layer is not seen in MYs 35 and 36, despite having had excellent coverage with ACS (see Figure S4 in Supporting Information S1). This indicates that any HCl present over this period was below a detection limit of 0.2–0.5 ppbv. In these MYs we still see widespread HCl detections occurring later in the season.

HCl in the southern hemisphere is very dynamic. We are able to make sporadic detections of low abundances between $L_s = 180°$ and 230° each year. The low number of detections in MY 34 is attributed to the GDS and its aftermath which prevented occultation measurements below 30 km for much of this period at most latitudes (Korablev et al., 2021). From $L_s = 230°$ to 290°, we observe abundances of 2.5–3.5 ppbv at higher altitudes around 40 km. Lower abundances, on the order of 1 ppbv, are seen below.

The lower altitude limits of the observations are caused by increasing aerosol loading toward the surface. Trends are visible in the data, and this is due to the variation in latitudes of ACS MIR occultation opportunities (see Figure 1 and Figure S4 in Supporting Information S1). Closer to the gaps in coverage surrounding $L_s = 250°$ and 280° in panels c and e of Figure 3, the lowest altitudes available are ∼20 km. These observations correspond to low latitudes as the occultation coverage approaches the equator. The vertical coverage extends to 5 or 10 km further from these gaps, where ACS MIR occultations are made at far southern latitudes between 60°S and 70°S.

As we approach $L_s = 300°$ in MYs 35 and 36 (Figures 3c and 3e) we see a sharp decrease in the altitude of peak HCl. VMRs at this time of year are the highest observed, between 3 and 5 ppbv, with the altitudes of peak abundances decreasing steadily over time. The gaps in L_s coverage are unfortunate, but combining the

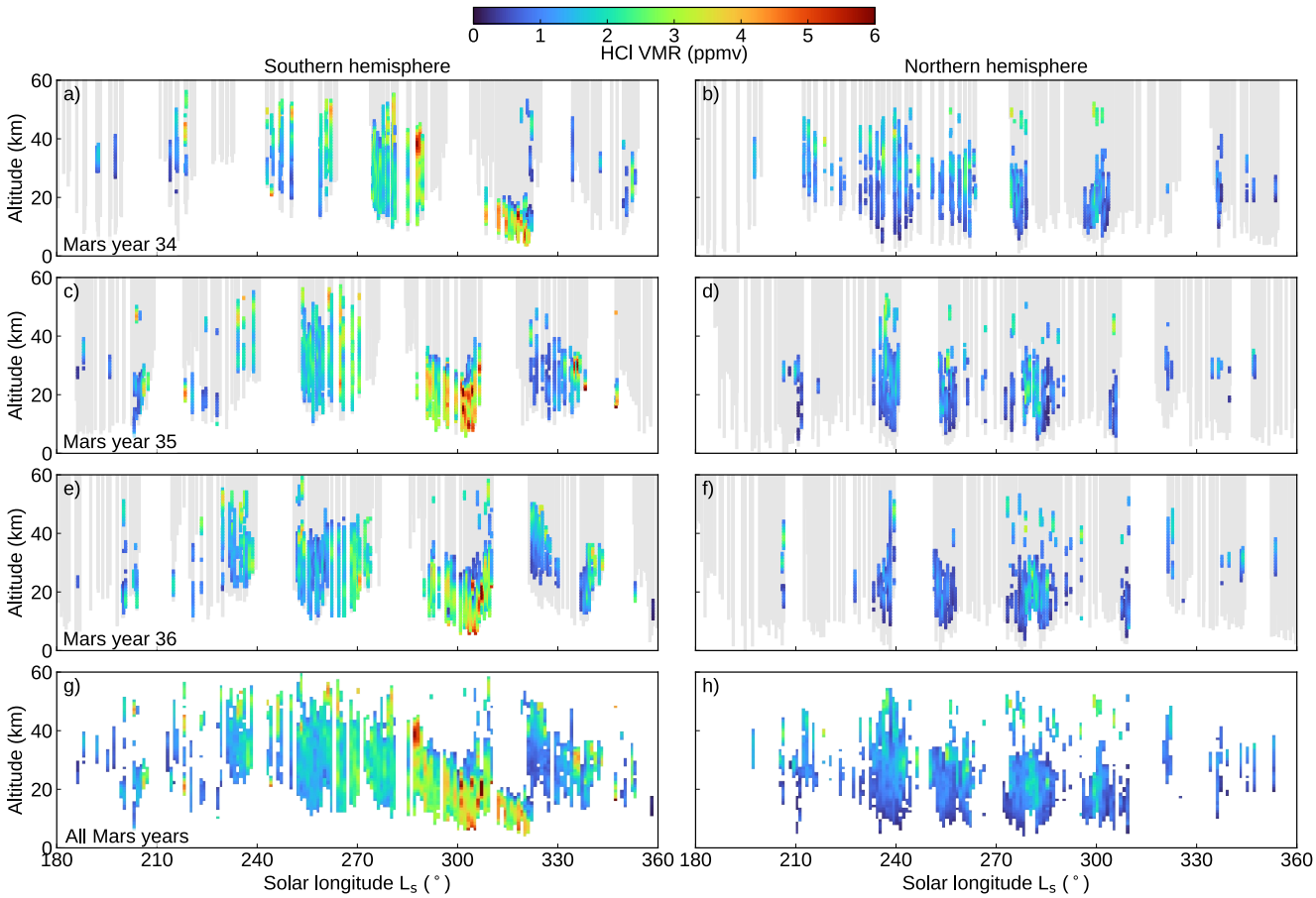

Figure 3. Climatology of HCl. Shown are vertical profiles of HCl VMR measured using ACS MIR as a function of solar longitude (L_s). Each row of panels represents a different Mars year (MY) from 34 (a, b) to 36 (e, f). The bottom row (g, h) combines all three MYs. Columns to the left (a, c, e) show observation made in the southern hemisphere, and panels on the right (b, d, f) show observations made in the northern hemisphere. Gray shading indicates periods and altitudes where secondary grating positions 11 and 12 were used, but the VMR of HCl was below the detection threshold. The latitudes of the ACS MIR observations covered in each panel are shown in Figure S4 in Supporting Information S1, which reproduces data from Figure 1.

observation in all three MYs paints a clear picture. In MY 34 (Figure 3a), we find a maximum abundance around 40 km at L_s = 285°. In MYs 34 and 35 (Figures 3c and 3e), the peak altitude has fallen to 30 km by L_s = 290°, and continues to fall steadily to <20 km by L_s = 305°. Returning to MY 34, this trend continues all the way until L_s = 320°, where the height of the HCl maxima is reduced to 10 km. While the latitudes of our observations change over L_s (see Figure S4 in Supporting Information S1) and impacts gas abundance, the overall trend described between L_s = 210°–340°, occurs over mainly over a latitude band between 40°S–60°S.

This trend is ended by the onset of the annually occurring late-season dust storm (often called "C storms" after Kass et al. (2016)). In MY 34, the late-season storm occurs much later than in MYs 35 and 36, around L_s = 320°, after we have seen the HCl peak-height fall to 10 km. This is shown in Section 4.3 and Figure 5 using MCS data. In MYs 35 and 36, the onset of the late-season storm is around L_s = 310° to 315°, periods in which we were still making ACS MIR observations at low latitudes before the beta angle prevented occultations. At these times we see a sudden increase in the altitudes at which HCl can be detected. This is most likely due to the storm activity which is preceded by the elevation of water vapor and rapidly rising atmospheric temperatures associated with seasonal dust activity. The late-season dust storm also affects the ACS solar occultation observations of temperature and water vapor, which will be presented in the following sections.

After the late-season dust storms, only low abundances of HCl are observed, and only at altitudes above the height of the remnants of the dust storm. Over time, the altitude range of detected HCl decreases, indicating that

abundances in the upper observed altitudes are falling off. Finally, after L_s = 340°, HCl detections become sporadic again as the southern autumnal equinox approaches.

In panels g and h of Figure 3 we have combined data from all three MYs. This is facilitated by the seasonal reproducibility of HCl and fills in the gaps in data caused by unfavorable beta angles. For each hemisphere, ACS MIR measurements are averaged on each L_s. Panel g, for the southern hemisphere, clearly shows the overall seasonal trend in HCl behavior, revealing its gradual change in altitude over time and the impacts of the early and late dust storms.

4.2. ACS and MCS Climatologies

Using the limb observations from MCS and the solar occultations of ACS MIR, we have a clear picture of the climatological trends in the vertical distributions of several quantities that change alongside HCl, and will help explain the observed variations in HCl. In the following sections, we will examine the repeating seasonal changes in the vertical structures of dust and its impact on temperatures. These, in turn, control the abundances of water vapor and water ice, which we will show impact the VMR of HCl.

For example, Figure 4 shows the vertical distribution changing over L_s for each of those quantities during southern spring and summer in MY 35. MCS data are zonally averaged between 40°S and 60°S where the majority of southern ACS MIR occultations are made in Figure 3. The MCS dust opacity (Figure 4a) shows a slight increase in activity around L_s = 210°, followed by the onset of a seasonal regional dust storm lasting from around L_s = 230° to 250°. Elevated dust levels persist through L_s = 300° before visibly subsiding. At L_s = 315°, a second seasonal storm occurs with a more punctuated onset. Dust is lofted above 30 km, but a decrease in opacities is seen between 5 and 20 km. The dust raised by the late-season storm falls off almost exponentially and subsides before the southern autumnal equinox.

The temperatures measured with MCS (Figure 4b; zonally averaged) follow the vertical distribution of dust very closely. Temperatures in the upper altitudes are shown in Figure 4 are <175 K. Below the top of the observations of elevated dust, we observe a band that has warmed up to 200 K. Such an isotherm first rises at L_s = 210° above 20 km, and then climbs above 50 km during the regional dust storm around L_s = 230°. It remains in place around 30 km throughout most of the perihelion period but falls after L_s = 300°. It rapidly climbs again to 60 km during the late-season storm at L_s = 315°, falling again before the equinox.

The water ice opacity measured with MCS (Figure 4c; zonally averaged) is generally very low at all altitudes (<0.001 km^{-1}). There is a water ice layer that corresponds to a ∼175 K isotherm throughout the season, with very low abundances above, where there is little water vapor to form ices, and below, where temperatures are too warm for the ice phase. This roughly corresponds to the hygropause height, which is a limit in the vertical extent of water vapor controlled by temperature (Liuzzi et al., 2020). The altitude level of the ice layer is clearly controlled by the atmospheric temperatures, which themselves follow the heights reached by dust.

Figure 4d shows water vapor measured with ACS NIR. These data are restricted to the ACS tangent locations whose latitude changes over time, as shows in Figure 1, whereas the MCS data are zonally averaged. Around L_s = 210°, we observe initial seasonal increases in water vapor from the surface to 40 km. These observations correspond to equatorial crossings in the tangent location and reflect latitudinal variations. This is consistent with early seasonal dust lifting and atmospheric warming. After L_s = 230°, a regional dust storm has started and we observe a rapid increase in the hygropause height to above 60 km, and this remains the case through L_s = 280°, consistent with MCS observations of dust and temperature (see also Fedorova et al. (2020, 2023) for a comparison of ACS NIR water vapor and temperature at the tangent locations). Between L_s = 290° and 310°, a steady decline in the vertical extent of water vapor is seen in the lead up to the late-season storm, driven by cooling atmospheric temperatures following perihelion. This period features the highest concentrations of atmospheric water vapor. Following the late-season storm, we again have an elevated hygropause, but with lower concentrations than during the nominal dusty period following the regional storm at L_s = 230°. Beyond L_s = 345°, water vapor is very abruptly removed from the atmosphere at these low southern latitudes. This is due to rapid cooling and contraction of the atmosphere following the late-season storm and leading into southern fall.

Atmospheric concentrations of observed HCl, shown in Figure 4e, closely match the behavior of water vapor. Early observations occur at low latitudes during the equatorial crossings around L_s = 210°, followed by a sharp increase in vertical extent and abundance after the onset of the regional dust storm at L_s = 230°. Approximately 2

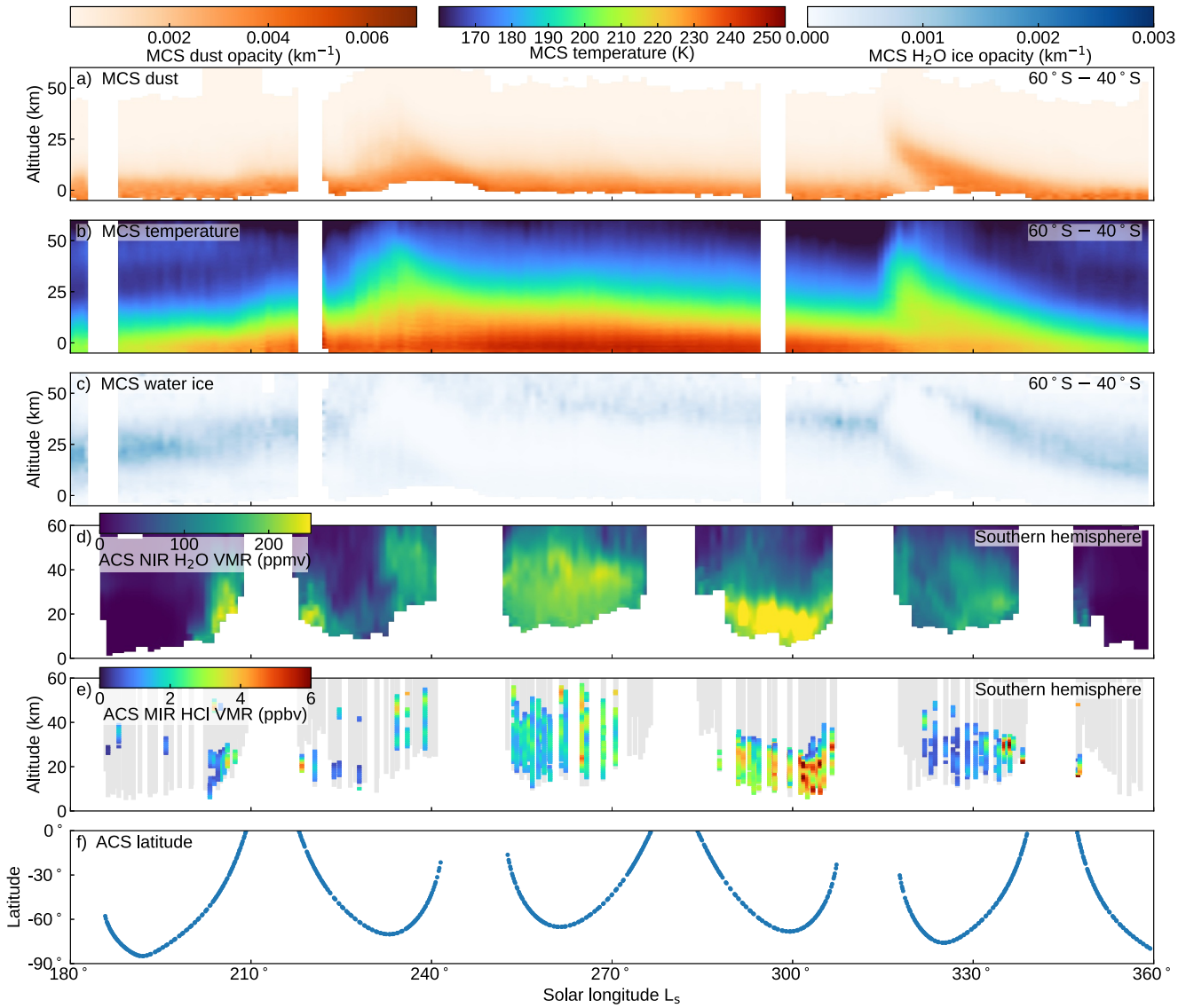

Figure 4. Example of the combined climatologies of dust, ice, temperature, H_2O, and HCl. For the southern hemisphere in MY 35, shown are: (a) the dust opacity from MCS, (b) temperatures from MCS, (c) water ice opacity from MCS, (d) water vapor VMR from ACS NIR, and (e) HCl VMR from ACS MIR. Panel (f) shows the ACS solar occultation latitudes as shown in Figure 1 and Figure S4 in Supporting Information S1. The MCS data shown are zonally averaged using measurements from a mid-latitude band covering 60°S to 40°S. All altitudes are relative to the Mars areoid. Gray shading indicates periods and altitudes where secondary grating positions 11 and 12 were used, but the VMR of HCl was below the detection threshold.

ppbv HCl is maintained through $L_s = 280°$ with a similar vertical limit as water vapor, which corresponds to the atmospheric temperatures and the ice condensation limit of water. After $L_s = 280°$, the vertical extent of HCl falls steadily, while its abundance grows to 3–4 ppbv. After the late-season dust storm, we make consistent HCl observations with a low abundance, but wide vertical extent, until around $L_s = 245°$, after which only sporadic observations with low confidence are made.

Versions of Figure 4 for MYs 34 and 36 are provided in Supporting Information S1 (Figures S5 and S6). Similar figures displaying observations made over the northern hemisphere during MYs 34–36 are provided as Figures S7–S9 in Supporting Information S1. These data, for each MY and hemisphere are arranged as in Figure 3 is presented in the following sections.

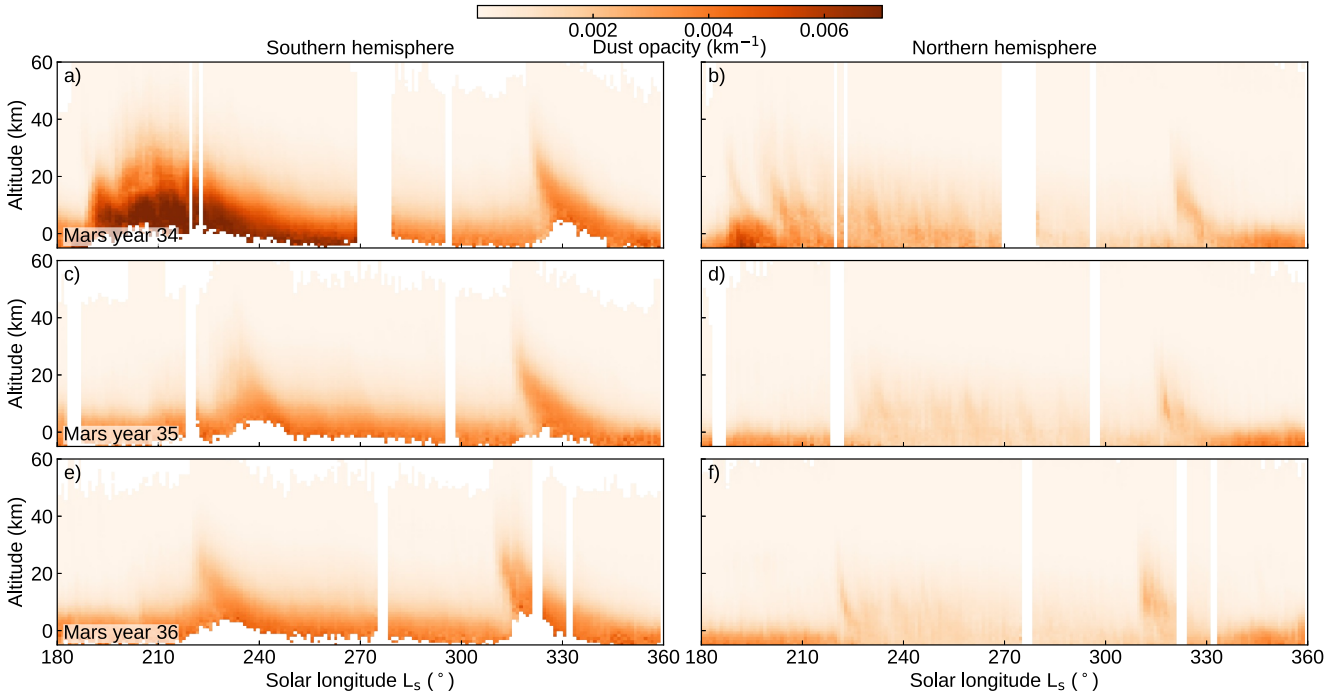

Figure 5. Climatology of dust opacity measured with MCS. Shown are vertical profiles of dust opacity per km measured with MCS as a function of L_s. MCS data are zonally averaged over latitude bands of 40°N to 60°N for the northern hemisphere, and 60°S to 40°S for the southern hemisphere. Panel arrangements by Mars year and hemisphere are as in Figure 3.

4.3. Dust

In Figure 5, we show the changes in the vertical distribution of dust measured with MCS over time. As in Figure 4a, the MCS observations are zonally averaged over a band covering either 60∘S to 40∘S or 40∘N to 60∘N. The figure panels are divided in northern and southern hemispheres, and by Mars year. Figure 5 is reproduced as Figure S10 in Supporting Information S1 with MCS data restricted to where co-locations were found with ACS solar occultations.

The top panels (Figures 5a and 5b) show MY 34 which was dominated by the GDS. A sharp increase in dust opacity over altitude from the surface to >30 km can be seen between L_s = 185° and 190°. This is most pronounced in the southern hemisphere, where we see the highest opacities out of any MY. In the south, the impact of the GDS, elevated dust opacities over a wide range of altitudes, last well after L_s = 250°, although the planet-encircling phase of the initiating GDS event is considered to only last through L_s = 205°–215° (Guzewich et al., 2019; Kass et al., 2019). In this main phase of the GDS, dust was lifted to above 80 km (Kass et al., 2019).

In the northern hemisphere, the initial phase of the GDS is seen as a rapid pulse in Figure 5b, followed by several additional phases of growth and decay (see, e.g. Guzewich et al., 2019; Kass et al., 2019). Significantly elevated dust opacities throughout the 0–30 km altitude range relative to MYs 35 and 36 (Figures 5d and 5f) are observed from L_s = 210° to 270°.

MYs 35 and 36 are examples of typical Martian seasonal dust activity (Montabone et al., 2015). In the southern hemisphere (Figures 5c and 5e), the average dust opacities increase after L_s = 210° due to large, but regional, dust storms. This lifting phase occurs midway between the vernal equinox (L_s = 180°) and the perihelion point (L_s = 251°), and a decay phase begins between the perihelion and summer solstice (L_s = 270°).

This is less pronounced in the northern hemisphere (Figures 5d and 5f), which is characteristically absent of clear growth and decay phases. The initial dust lifting after L_s = 220° is pronounced, and a clear lifting of dust to well above 30 km is observed. After this, the dust opacities remain somewhat constant through the majority of the period, with a gradual decay in the maximum vertical extent.

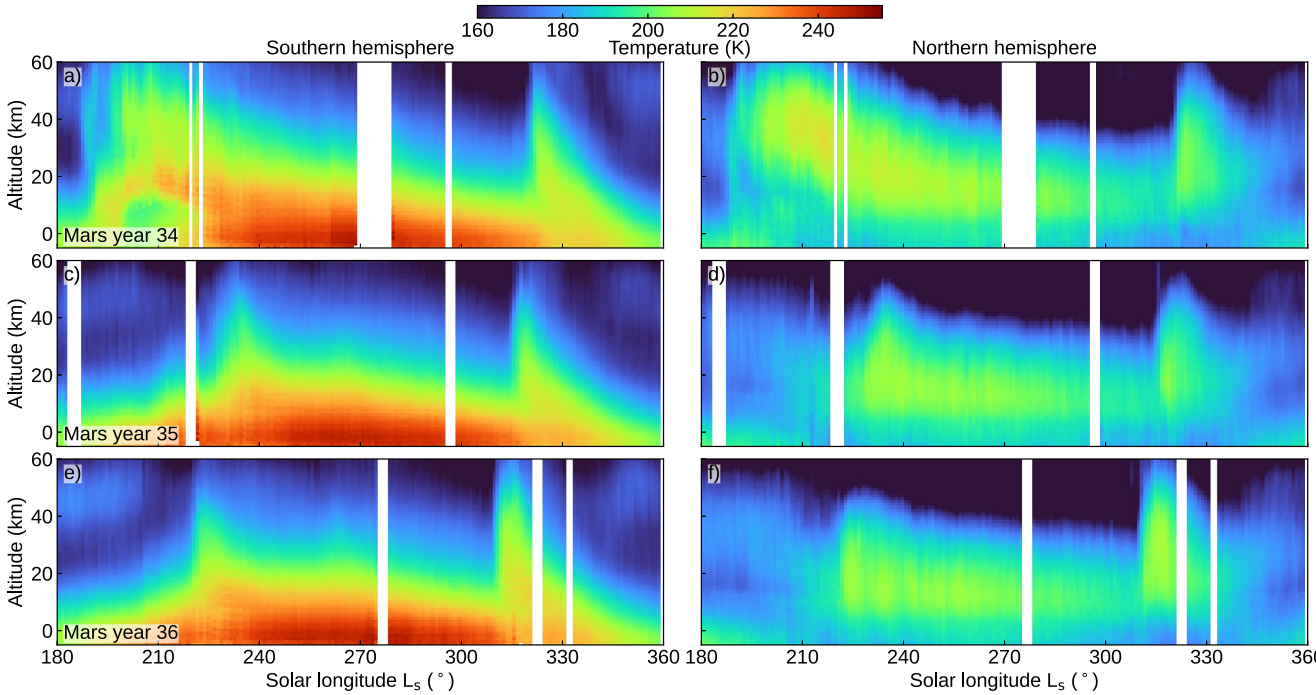

Figure 6. Climatology of temperature measured with MCS. Shown are vertical profiles of temperature measured with MCS as a function of L_s. MCS data are zonally averaged over latitude bands of 40°N to 60°N for the northern hemisphere, and 60°S to 40°S for the southern hemisphere. Panel arrangements by Mars year and hemisphere are as in Figure 3. Temperature measurements made using ACS NIR for the corresponding periods are shown in Figure S13 in Supporting Information S1.

In all MYs, the observed dust activity is punctuated by a late-season storm, seen clearly in both hemispheres. These occur between $L_s = 310°–330°$, are seen to occur progressively earlier in the season from MY 34–36. These late-season storms are characterized by a very sudden lifting of dust to 40–50 km, followed by a rapid decay. By $L_s = 330°–345°$, dust activity is almost completely subsided, with elevated opacities restricted to <10 km. This level and vertical extent of dust remains throughout the aphelion period (southern fall and winter) from $L_s = 0°–180°$.

4.4. Temperature

When dust is lifted into the Martian atmosphere, it has a positive feedback on atmospheric temperatures by both absorbing and scattering incoming solar infrared radiation (e.g., Madeleine et al., 2011; Pollack et al., 1979; Smith et al., 2001). This is clearly seen in the MCS data when comparing the panels in Figure 5, showing dust opacity, with those in Figure 6, which show temperatures (MCS data are zonally averaged over a latitude band covering 60°S to 40°S). The zonally averaged data in Figure 6 are not limited by local time, as the ACS data will comprise of both morning and evening terminator observations. When zonally averaged over this L_s range, southern hemisphere MCS temperatures recorded in the afternoon/evening are significantly warmer than those at night/morning. Figure 6 is reproduced in Figures S11 and S12 in Supporting Information S1 to show the afternoon and night MCS temperature data.

Shortly after the southern vernal equinox in MY 34 (Figures 6a and 6b), there is a rapid warming of the lower atmosphere that coincides with the start of the GDS. This is apparent in both the northern and southern hemisphere, and there is a visible link to the height at which dust is lifted. This is clearly visible in the vertical structure of temperatures right at the start of the GDS in which the initial phase at $L_s = 190°$ drives dust up to 25 km, which impacts atmospheric temperatures over the same altitude range. In the next phase of the GDS, after $L_s = 200°$, dust is driven well above 40 km and causes warming over the entire altitude range shown.

The dust activity during the GDS is of such severe intensity that the positive feedback mechanism between dust and temperature does not impact the entire atmosphere. At the peak of the GDS, the dust opacity grows large enough at a high enough altitude that the amount of infrared radiation reaching the lower atmosphere (below

20 km) is reduced overall, limiting the amount of the warming the atmosphere experiences, and even leading to a net cooling effect above the surface (Figures 6a and 6b). This is also seen in the ACS NIR temperature data (Fedorova et al., 2023).

In MYs 35 and 36, without the GDS, the warming of the atmosphere in the southern hemisphere tracks the growth of the regional dust storm activity. Increases in temperature from the surface to 10 km occur around $L_s = 210°$, but grow to cover altitudes from the surface to >40 km when the dust opacities sharply increase at $L_s = 230°$ and 220° for MY 35 and 36, respectively. In the northern hemisphere, the impact of warming is much weaker, corresponding to the relative decrease in the dust opacity. Dust over these periods (Figures 5d and 5f) exhibits a sudden lifting when the southern regional dust storms occur, which is observed as a decrease in dust opacity near the surface, and a moderate increase in opacity from the surface to well above 30 km. This lifted dust creates a warm layer in the atmosphere extending from 10 to 40 km, and lasting until the late-season dust storms. Just as for the dust opacity, the upper altitude of the warm layer decays over time between $L_s = 220°$–230° and $L_s = 310°$–320°. Toward the surface, the axial tilt of Mars controls solar insolation and results in a cold layer forming that is representative of the northern fall and winter seasons.

In all three MYs shown (34–36), the late-season dust storms clearly impact the vertical profiles of temperature. This is seen in all six panels of Figure 6 as a very sudden increase in temperatures from the surface to above 50 km at some point between $L_s = 310°$–330°. Just like the dust opacities following the late-season storm, the upper limit of the warming decays rapidly as the southern autumnal equinox approaches.

As in Figures 4 and 5, the temperature data measured with MCS and shown in Figure 6 are zonally averaged over latitude bands. Vertical profiles of temperature measured with ACS NIR at the locations of TGO solar occultation opportunities over the same period (Fedorova et al., 2020, 2023), and arranged in the same manner, are shown in Figure S13 in Supporting Information S1. Overall, the magnitudes and trends in temperature are consistent between MCS and ACS NIR. Differences seen in Figure S13 in Supporting Information S1 are largely a result of the variability of latitude over time that is a restriction of the solar occultation technique (see Figure S4 in Supporting Information S1). Vertical profiles of temperature measured with MCS only where co-locations with ACS solar occultations are shown in Figure S14 in Supporting Information S1, arranged in the same manner. Quantitative validations of the temperature data products from ACS NIR and MCS are provided in Fedorova et al. (2020) and part 2 of this study (Olsen et al., 2024b). A critical result that came from ACS NIR was the frequent detection of layers of the atmosphere featuring water vapor supersaturation (Fedorova et al., 2020, 2023). The relationship between supersaturation and HCl is not assessed since HCl observations, restricted by the relatively low abundance of HCl and the sensitivity of ACS MIR, are only made below the hygropause, and therefore below where supersaturation is observed.

4.5. Water Ice

The vertical distribution of water ice opacity over L_s for the southern and northern hemispheres and for MYs 34–36 are shown in Figure 7, arranged as in Figure 3. The MCS water ice opacities are zonally averaged over a latitude band covering 60°S to 40°S, as shown in Figure 4c. Figure 7 is reproduced as Figure S15 in Supporting Information S1 with MCS data restricted to where co-locations were found with ACS solar occultations. In contrast to the dust opacity, the distribution of water ice over the perihelion period is characterized by a lack of ice formation throughout the lower atmosphere during the perihelion period. This is, of course, driven by the dust-induced warming over the altitude and L_s range shown.

In all six panels of Figure 7, the sudden warming caused by intense dust activity is visible as an acute, rapid decrease in water ice. Such events include the GDS in MY 34, regional storms after $L_s = 210°$ in MYs 35 and 36, or the late-season storms in each MY occurring after $L_s = 310°$. At the start of the perihelion period, the southern vernal equinox, water ice may be present, on average at most latitudes, with a band of high opacity visible at 25 km at southern latitudes, and a lower-opacity band visible at 20 km at northern latitudes. With the exception of MY 34, as spring begins in the southern hemisphere, the height of this initial water ice layer increases, while the mean opacity of water ice decreases. When the regional dust storms begin ($L_s = 230°$ and 220° for MY 35 and 36, respectively), the signature of water ice is reduced at all altitudes almost completely. Between $L_s = 240°$ and 310°, there is evidence of the presence of water ice above 60 km, and gradually falling to 40 km, until the late-season dust storms produce a second rapid warming throughout the altitude range shown. Following these dust event, elevated water ice opacity becomes visible again at 60 km, decaying very rapidly to below 20 km.

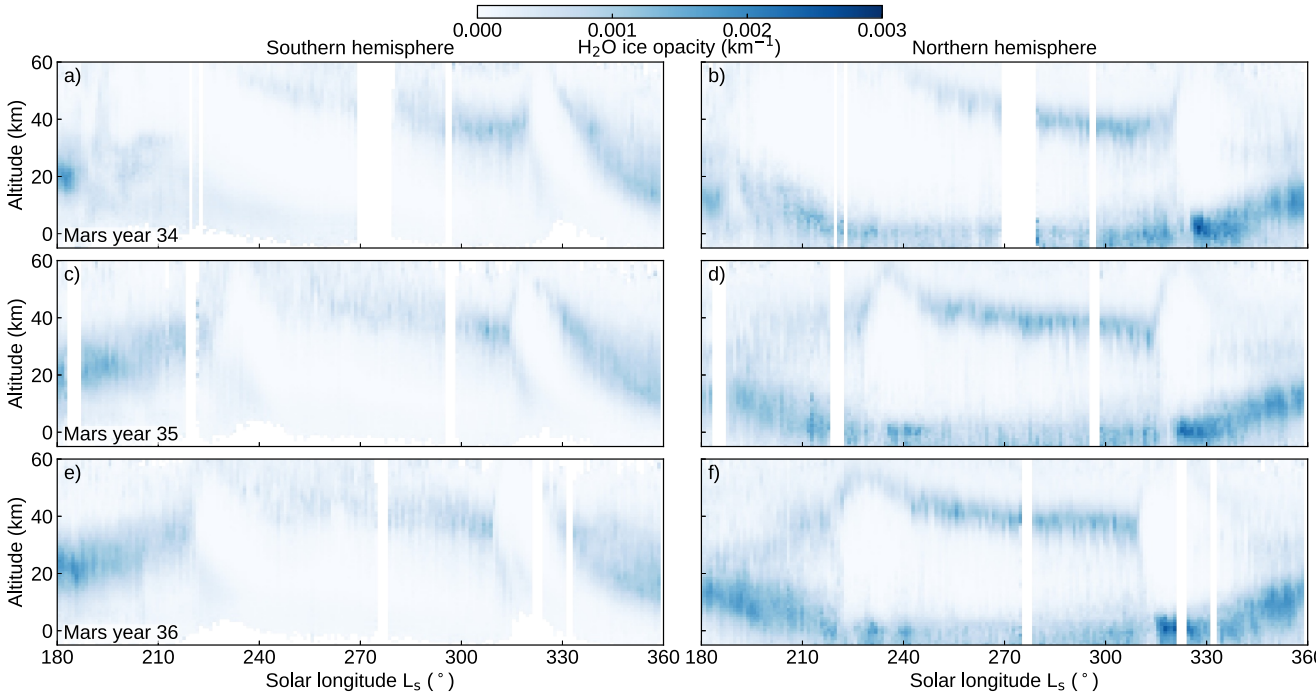

Figure 7. Climatology of water ice opacity measured with MCS. Shown are vertical profiles of water ice opacity measured with MCS as a function of L_s. MCS data are zonally averaged over latitude bands of 40°N to 60°N for the northern hemisphere, and 60°S to 40°S for the southern hemisphere. Panel arrangements by Mars year and hemisphere are as in Figure 3.

Some of the features of the southern hemisphere climate described above are also visible in the northern hemisphere. These are the impacts of the dust events, and the water ice layer present between 60 and 40 km in the period between the seasonal dust storms (L_s = 240–310°). Unique to the northern hemisphere is the presence of water ice below 10 km. This is caused by a cold air mass close to the surface that has reduced insolation due to Mars' axial tilt. The latitude bands covered in the averaged MCS data partially cover the northern polar hood, which forms during northern fall and winter and has a maximum extent between L_s = 200–320°, extending south as far as 40–45∘N (Giuranna et al., 2021; Olsen, Forget, et al., 2021; Smith, 2004; Willame et al., 2017).

The contours of water ice opacity shown in Figure 7 are strongly dependent on atmospheric temperature. In comparison to Figure 6, the location of the bands of highest water ice opacity appear to follow an isotherm of around 170–180 K (dark blue color in Figure 6). Close inspection will reveal that low-altitude formations in the northern hemisphere after L_s = 315° is coincident with slightly warmer atmospheric temperatures, while the high-altitude formations in the northern hemisphere occur at slightly colder temperatures. In part 2, we will show that water ice occurs over a wide temperature range (using the vertical profiles of individual measurements, rather than data that has been zonally averaged), but that ice falls off rapidly above 180 K (Olsen et al., 2024b).

4.6. Water Vapor

Finally, water vapor measured with ACS NIR and ACS MIR is shown in Figure 8. Since the ACS solar occultations are much more sparse than the MCS measurements, the data are shown for all latitudes covered with minimal averaging. The variation of latitudes over L_s corresponding to the observations shown in Figure 8 is given in Figure S4 in Supporting Information S1. Data are binned into 1° divisions of L_s and averaged. Water vapor VMR vertical profiles retrieved from ACS NIR solar occultations are only available at the time of writing through the aphelion period of MY 36 and were previously reported in (Fedorova et al., 2023). The panels in Figure 8 corresponding to the perihelion period of MY 36 (e and f) contain water vapor VMR vertical profiles retrieved from ACS MIR. The ACS MIR observations were made using secondary grating positions 11 and 12 and are coincident with the HCl measurements shown in Figure 3. There is good agreement between the ACS MIR and ACS NIR H_2O measurements (quantified in part 2 Olsen et al., 2024b), although the ACS MIR data are more sparse. All three MYs of ACS MIR water vapor VMR vertical profiles are shown in Figure S16 in

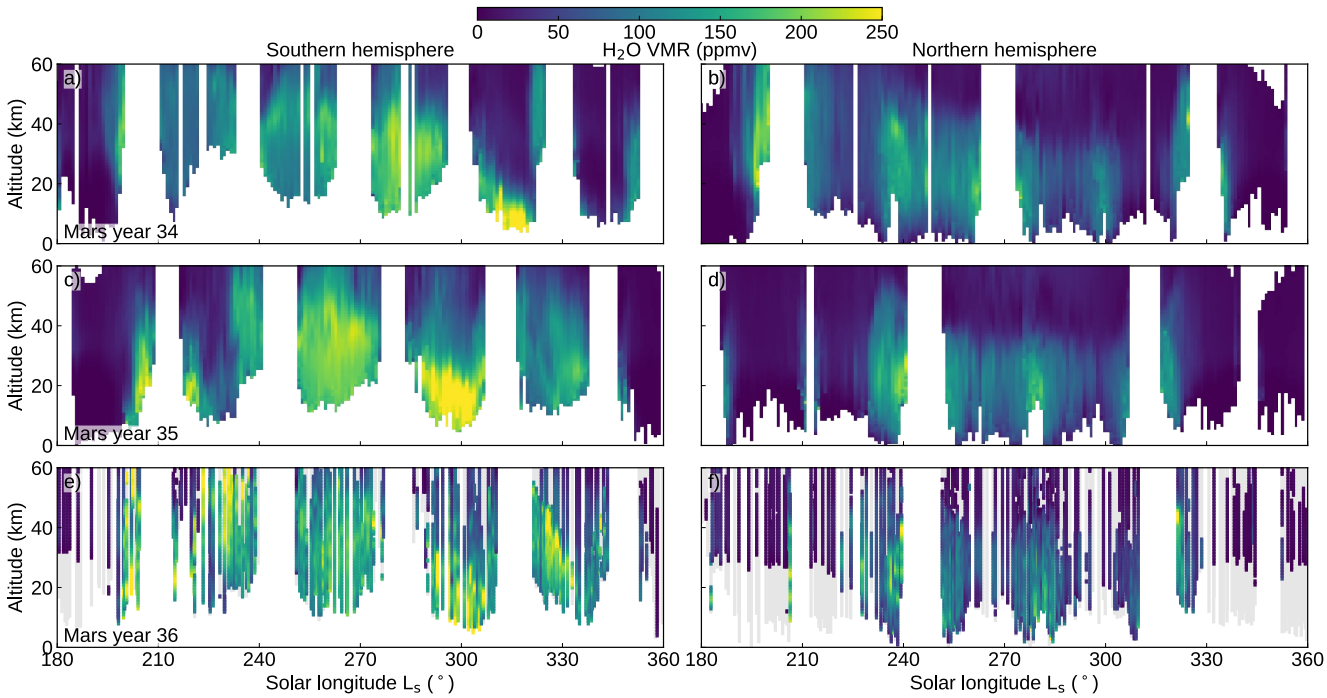

Figure 8. Climatology of water vapor measured with ACS NIR. Shown are vertical profiles of H_2O VMR measured using ACS NIR or ACS MIR as a function of L_s. Panel arrangements by Mars year and hemisphere are as in Figure 3. ACS NIR data are shown for MYs 34 and 35, but was not yet available over the perihelion period of MY 36. ACS MIR data are shown for MY 36. ACS MIR data for the corresponding periods over all MYs is shown in Figure S16 in Supporting Information S1. The latitudes of the ACS MIR observations covered in each panel are shown in Figure S4 in Supporting Information S1, which reproduces data from Figure 1. Gray shading indicates periods and altitudes where secondary grating positions 11 and 12 were used, but the VMR of H_2O was below the detection threshold.

Supporting Information S1. Thorough discussions of the observations of water vapor made with ACS are provided in Fedorova et al. (2020, 2023).

In the southern hemisphere, we observe a very dry atmosphere following the southern summer equinox, as the whole atmosphere remains impacted by the previous southern winter. In MY 34, the impact of the GDS, and resulting warming, is observed around $L_s = 190°$ as elevated VMRs between 20 and 60 km in both hemispheres. In MY 35, the impact of the regional dust storm is seen later in the season, corresponding to the later dust activity; with H_2O reaching lower altitudes; and with far less impact in the northern hemisphere solar occultations. Following the acute dust storms, we see elevated water vapor VMRs throughout the majority of the perihelion period. This occurs in concert with HCl (Figure 3). The hygropause is elevated at certain times and latitudes to well above 60 km. As we saw in the HCl VMRs, dust opacities, temperatures, and water ice opacities, the hygropause gradually decreases between $L_s = 220°$ and 320°. Unlike with the dust opacity and temperature, the decrease in the hygropause is accompanied by increasing H_2O VMRs, with the maxima reached around $L_s = 315°$ in MY 34 and between $L_s = 290°$ and 310° in MYs 35 and 36. These maxima occur below 20 km and similar behavior is seen in the HCl data shown in Figure 3.

The solar occultation data reveal a strong latitudinal dependence on the impact of the late-season storms. In the southern hemisphere in MY 34 (Figure 8a), elevated water is seen reaching above 60 km, and is correspondingly visible in the northern hemisphere. These data, near $L_s = 340°$, were made at very low latitudes and are adjacent to a period of unfavorable beta angles making solar occultations impossible. Conversely, the period over which the MY 35 and 36 late-season storms were observed occur at very high latitudes in both hemispheres. Elevated H_2O VMRs are observed in the southern hemisphere, where the dust intensity and temperatures are much higher, while very little water vapor is seen at the high northern latitudes beyond $L_s = 330°$.

In the northern hemisphere, over the periods between dust events, we see elevated H_2O VMRs from 10 to 50 km, although with lower magnitudes than in the southern hemisphere. Over this time frame ($L_s = 220°$–320°), the hygropause appears to decrease in altitude see Holmes et al. (2024). This is especially apparent in MY 34, but in all MYs examined the H_2O VMR is strongly impacted by the latitudes that are varying with L_s, with larger VMRs,

and corresponding higher hygropause levels, occurring at low latitudes (see Figure S4 in Supporting Information S1). This overall trend is in agreement with that seen in each other variable: HCl VMR from ACS MIR; and the dust opacity, temperature, and water ice opacity from MCS.

With both solar occultation spectrometer suites on the ExoMars TGO, we have been able to monitor the Martian climate with unprecedented sensitivity on the vertical scale and unprecedented sensitivity to water vapor. We have shown how water vapor reacts to global dust storms (Brines et al., 2023; Fedorova et al., 2020); how atmospheric water vapor cycles between seasons in both hemispheres (Aoki et al., 2022; Fedorova et al., 2023); how the distribution of HDO and the deuterium-to-hydrogen ratio varies with height and season (Alday et al., 2021; Villanueva et al., 2021); and how water vapor can be injected far above the hygropause during the dusty periods (Belyaev et al., 2021; Fedorova et al., 2020). This work, and part 2 (Olsen et al., 2024b), is the first comprehensive analysis of water vapor when compared to temperature, water ice, dust, and HCl. Following Olsen et al. (2022), where temperature, H_2O, and O_3 were compared over altitude, we have shown that the abundances of water vapor and water ice in the Martian atmosphere are controlled by changes in the atmospheric temperature, and that temperatures are driven by dust loading. Furthermore, the data sets presented here include the most up-to-date water vapor and HCl retrievals from TGO, with the perihelion water vapor data products derived from ACS MIR secondary grating positions 11 and 12 having been presented for the first time.

5. Conclusion

In every quantity examined, we observe similar seasonal trends, all linked to Mars' orbit and a cascading collection of linked physical mechanisms. Southern spring is initiated and driven two-fold: by the decreased distance between the Sun and Mars and an axial tilt that brings the sub-solar point south toward the pole. The result is a warming of the surface and atmosphere, sublimation of water and CO_2 on the southern polar cap, and increased atmospheric density and surface pressure. This leads to dust lifting and atmospheric warming. The expansion of the lower atmosphere elevates the hygropause and brings water vapor to higher altitudes.

The seasonality of the Martian atmosphere has been well observed over time, from the Earth, from nadir-pointing instruments, and from limb-viewing instruments that provide access to the vertical structure of temperature, pressure, and gas abundance. The ExoMars Trace Gas Orbiter has greatly improved our capabilities to investigate the Martian atmosphere across all scales in terms of sensitivity and coverage. This study brought together the dust and water ice aerosols opacities measured with the Mars Climate Sounder on MRO with those of the abundances of water vapor and hydrogen chloride made with the Atmospheric Chemistry Suite on TGO. MCS is limb-viewing, has excellent vertical resolution, and high-density data coverage. ACS used the solar occultation technique, has very high sensitivity to trace gas abundance and their variations along the vertical, but is much more restricted in its coverage. The seasonal evolution of temperature, dust, water ice, and water vapor have been described previously for each instrument, but this is the first comprehensive comparison of multiple measured quantities between TGO and MRO, and the first description of the seasonality of HCl, and how it compares to the other quantities.

HCl, the novel aspect of this investigation, is certainly affected dynamically and photochemically by the activities resulting from the southern spring and summer seasons. In this paper we have shown how dust lifting impacts atmospheric temperatures, which drive water vapor to higher altitudes and define the altitudes where water ice forms. The vertical extent of each parameter is linked in each Mars year observed, with the extent of dust lifting governing the heights where warming occurs, which defines the hygropause height and layer of water ice just above. Key dust events, the magnitude and timing of which is unique each year, are seen to affect all parameters consistently, with early season and late-season dust storms leading to rapid increases of all parameters over a wide altitude range. At either end of the season, this is followed by a decay phase which is slow at the end of southern spring, while the atmosphere is being driven by perihelion solar insolation and optimal axial tilt, but very rapid at the end of southern summer when this is no longer the case.

HCl is shown to closely follow the behavior of water vapor in both its vertical extent, changes over time, and even its relative abundance. This is expected behavior for HCl since its most rapid formation mechanism should be via the reaction with water vapor photolysis products. However, HCl was also expected to be a stable reservoir for atmospheric chlorine. We also show that the extent of HCl follows those of the compared aerosols, occurring in the presence of dust, and at altitudes with little water ice. This reinforces hypotheses about dust being an HCl source, whether direct or indirect.

While this study strongly suggests that the availability of water vapor controls the production rate of HCl, we do not know what the source of free Cl is for this production. While possibilities include the temporally correlated lifted dust, or some sort of surface emission related to changes in frost cover, the rapid loss mechanisms also remain unknown. HCl is not condensible like water vapor and a change in its production mechanism at the end of the dusty season still requires a reservoir to sequester the remaining chlorine.

In part 2 of this investigation, we quantify the correlations and anti-correlations between each parameter along the vertical (Olsen et al., 2024b). We show that HCl abundances track those of water vapor very closely in vertical extent and over time; that both gases are controlled by temperature, impacting the hygropause height and water ice formation; and that dust lifting drives changes in temperature. This comparison provides constraint to the likelihood and feasibility of each production and destruction mechanism that we have so far considered. The paper will conclude with an in depth discussion of such mechanisms and comment on their importance and any potential issues they have.

Conflict of Interest

The authors declare no conflicts of interest relevant to this study.

Acknowledgments
This work was funded by the UK Space Agency (ST/T002069/1, ST/Y000196/1). The ExoMars mission is a joint mission of the European Space Agency (ESA) and Roscosmos. The ACS investigation was developed by the Laboratoire Atmosphères, Milieux, Observations Spatiales (LATMOS/CNRS) in Paris and the Space Research Institute (IKI) in Moscow. The investigation was funded by the National Centre for Space Studies of France (CNES) and Roscosmos. The GGG software suite is maintained at JPL (tccon-wiki.caltech.edu). IKI affiliates acknowledge funding from the Ministry of Science and Higher education of the Russian Federation. LATMOS affiliates acknowledge funding from CNES and ANR (PRCI, CE31 AAPG2019-MCUBE project). Open University affiliates acknowledge funding from the UK Space Agency (ST/V002295/1, ST/W00268X/1, ST/W002949/1, ST/V002295/1, ST/V005332/1, ST/X006549/1 and ST/Y000234/1. Work at the Jet Propulsion Laboratory, California Institute of Technology, was performed under contract with the National Aeronautics and Space Administration (80NM0018D0004). MCS data and assistance were provided by D.M. K. and A.K. and additional processing was performed by P.S. and J.A.H. All spectral fitting of ACS MIR data was performed by K.S.O. using the GGG software suite. Temperature and pressure data from ACS NIR were provided by A.A.F. Processing of ACS spectra is done by A.T. at IKI and by L.B. at LATMOS by L.B. Input and aid on spectral fitting, and on interpretation of data, were given by J.A., D.A.B., A.A.F., F.M., F.L., M.R.P., and J.M. Atmospheric modelling and insight into atmospheric chemistry were performed by K.R. and P. S. The ACS instrument was designed, developed, and operated by A.P., A.S., A. T., F.M., and O.K. We would like to thank Duhita Naware and Mhairi Reid for consulting on color schemes and Glenn Orton for kindly reviewing our manuscript prior to submission.

Data Availability Statement

The VMR vertical profiles generated in this study are available on the Oxford Research Archive (Olsen et al., 2024a). The data sets generated by the ExoMars Trace Gas Orbiter instruments analyzed in this study are made available in the European Space Agency (ESA) Planetary Science Archive (PSA) repository (European Space Agency, 2023), following a 6 months prior access period, and the ESA Rules on Information, Data and Intellectual Property. Temperature and pressure data used here are from ACS NIR and were generated in other studies: data from MY 34 are made available in Fedorova et al. (2020) and an updated data version containing MYs 34–36 are published in Fedorova et al. (2023). Data from the MCS investigation (v5.2) are made available through the NASA Planetary Data System (PDS; NASA, 2017). The LMD MCD v5.3 and v6.1, as well as data generated with the PCM for TGO solar occultations, along with its user guide, are hosted by LMD (LMD, 2018).

References

Alday, J., Trokhimovskiy, A., Irwin, P. G. J., Wilson, C. F., Montmessin, F., Lefévre, F., et al. (2021). Isotopic fractionation of water and its photolytic products in the atmosphere of Mars. *Nature Astronomy*, *5*(9), 943–950. https://doi.org/10.1038/s41550-021-01389-x

Alday, J., Trokhimovskiy, A., Patel, M. R., Fedorova, A. A., Lefèvre, F., Montmessin, F., et al. (2023). Photochemical depletion of heavy CO isotopes in the martian atmosphere. *Nature Astronomy*, *7*(7), 867–876. https://doi.org/10.1038/s41550-023-01974-2

Aoki, S., Daerden, F., Viscardy, S., Thomas, I. R., Erwin, J. T., Robert, S., et al. (2021). Annual appearance of hydrogen chloride on Mars and a striking similarity with the water vapor vertical distribution observed by TGO/NOMAD. *Geophysical Research Letters*, *48*(11). https://doi.org/10.1029/2021gl092506

Aoki, S., Vandaele, A. C., Daerden, F., Villanueva, G. L., Liuzzi, G., Clancy, R. T., et al. (2022). Global vertical distribution of water vapor on Mars: Results from 3.5 years of ExoMars-TGO/NOMAD science operations. *Journal of Geophysical Research*, *127*(9). https://doi.org/10.1029/2022je007231

Belyaev, D. A., Fedorova, A. A., Trokhimovskiy, A., Alday, J., Montmessin, F., Korablev, O. I., et al. (2021). Revealing a high water abundance in the upper mesosphere of Mars with ACS onboard TGO. *Geophysical Research Letters*, *48*(10), e2021GL093411. https://doi.org/10.1029/2021GL093411

Brines, A., López-Valverde, M. A., Stolzenbach, A., Modak, A., Funke, B., Galindo, F. G., et al. (2023). Water vapor vertical distribution on Mars during perihelion season of MY 34 and MY 35 with ExoMars-TGO/NOMAD observations. *Journal of Geophysical Research*, *128*(11), e2022JE007273. https://doi.org/10.1029/2022JE007273

Devi, V. M., Benner, D. C., Sung, K., Crawford, T. J., Gamache, R. R., Renaud, C. L., et al. (2017). Line parameters for CO_2- and self-broadening in the ν_3 band of $HD^{16}O$. *Journal of Quantitative Spectroscopy & Radiative Transfer*, *203*, 158–174. https://doi.org/10.1016/j.jqsrt.2017.02.020

European Space Agency. (2023). ExoMars 2016 ACS calibrated data product collection (V104.1). [Dataset]. *European Space Agency*. https://doi.org/10.57780/ESA-RTLH14G

Fedorova, A. A., Montmessin, F., Korablev, O., Luginin, M., Trokhimovskiy, A., Belyaev, D. A., et al. (2020). Stormy water on Mars: The distribution and saturation of atmospheric water during the dusty season. *Science*, *367*(6475), 297–300. https://doi.org/10.1126/science.aay9522

Fedorova, A. A., Montmessin, F., Trokhimovskiy, A., Luginin, M., Korablev, O., Alday, J., et al. (2023). A two-Martian year survey of the water vapor saturation state on Mars based on ACS NIR/TGO occultations. *Journal of Geophysical Research*, *128*(1), e2022JE007348. https://doi.org/10.1029/2022JE007348

Forget, F., Hourdin, F., Fournier, R., Hourdin, C., Talagrand, O., Collins, M., et al. (1999). Improved general circulation models of the Martian atmosphere from the surface to above 80 km. *Journal of Geophysical Research*, *104*(E10), 24155–24176. https://doi.org/10.1029/1999JE001025

Gamache, R. R., Farese, M., & Renaud, C. L. (2016). A spectral line list for water isotopologues in the 1100–4100 cm^{-1} region for application to CO_2-rich planetary atmospheres. *Journal of Molecular Spectroscopy*, *326*, 144–150. https://doi.org/10.1016/j.jms.2015.09.001

Giuranna, M., Wolkenberg, P., Grassi, D., Aronica, A., Aoki, S., Scaccabarozzi, D., et al. (2021). The current weather and climate of Mars: 12 years of atmospheric monitoring by the planetary fourier spectrometer on Mars express. *Icarus*, *353*, 113406. https://doi.org/10.1016/j.icarus.2019.113406

Gordon, I. E., Rothman, L. S., Hargreaves, R. J., Hashemi, R., Karlovets, E. V., Skinner, F. M., et al. (2021). The HITRAN2020 molecular spectroscopic database. *Journal of Quantitative Spectroscopy and Radiative Transfer*, *277*, 107949. https://doi.org/10.1016/j.jqsrt.2021.107949

Graedel, T. E., & Keene, W. C. (1995). Tropospheric budget of reactive chlorine. *Global Biogeochemical Cycles*, *9*(1), 47–77. https://doi.org/10.1029/94GB03103

Guzewich, S. D., Lemmon, M., Smith, C. L., Martínez, G., Vicente-Retortillo, A. d., Newman, C. E., et al. (2019). Mars Science Laboratory observations of the 2018/Mars year 34 global dust storm. *Geophysical Research Letters*, *46*(1), 71–79. https://doi.org/10.1029/2018GL080839

Hartogh, P., Jarchow, C., Lellouch, E., Val-Borro, M. d., Rengel, M., Moreno, R., et al. (2010). Herschel/HIFI observations of Mars: First detection of O_2 at submillimetre wavelengths and upper limits on HCl and H_2O_2. Astron. *Astrophysica Norvegica*, *521*, L49. https://doi.org/10.1051/0004-6361/201015160

Holmes, J. A., Lewis, S. R., Patel, M. R., Alday, J., Olsen, K. S., Aoki, S., et al. (2024). Global mapping of the martian hygropause: Links to atmospheric dust and water loss. *Geophysical Research Letters*, *51*. https://doi.org/10.1029/2022JE007203

Irion, F. W., Gunson, M. R., Toon, G. C., Chang, A. Y., Eldering, A., Mahieu, E., et al. (2002). Atmospheric Trace Molecule Spectroscopy (ATMOS) experiment version 3 data retrievals. *Applied Optics*, *41*(33), 6968–6979. https://doi.org/10.1364/AO.41.006968

Kass, D. M., Kleinböhl, A., McCleese, D. J., Schofield, J. T., & Smith, M. D. (2016). Interannual similarity in the Martian atmosphere during the dust storm season. *Geophysical Research Letters*, *43*(12), 6111–6118. https://doi.org/10.1002/2016gl068978

Kass, D. M., Schofield, J. T., Kleinböhl, A., McCleese, D. J., Heavens, N. G., Shirley, J. H., & Steele, L. J. (2019). Mars Climate Sounder observation of Mars' 2018 global dust storm. *Journal of Geophysical Research*, *47*(23), e2019GL083931. https://doi.org/10.1029/2019GL083931

Keene, W. C., Khalil, M. A. K., Erickson, D. J., McCulloch, A., Graedel, T. E., Lobert, J. M., et al. (1999). Composite global emissions of reactive chlorine from anthropogenic and natural sources: Reactive Chlorine Emissions Inventory. *Journal of Geophysical Research*, *104*(D7), 8429–8440. https://doi.org/10.1029/1998jd100084

Kleinböhl, A., Friedson, A. J., & Schofield, J. T. (2017). Two-dimensional radiative transfer for the retrieval of limb emission measurements in the martian atmosphere. *Journal of Quantitative Spectroscopy & Radiative Transfer*, *187*, 511–522. https://doi.org/10.1016/j.jqsrt.2016.07.009

Kleinböhl, A., Schofield, J. T., Kass, D. M., Abdou, W. A., Backus, C. R., Sen, B., et al. (2009). Mars Climate Sounder limb profile retrieval of atmospheric temperature, pressure, and dust and water ice opacity. *Journal of Geophysical Research*, *114*(E13), E10006. https://doi.org/10.1029/2009JE003358

Kleinböhl, A., Spiga, A., Kass, D. M., J, H. S., Millour, E., Montabone, L., & Forget, F. (2020). Diurnal variations of dust during the 2018 global dust storm observed by the Mars climate sounder. *Journal of Geophysical Research*, *125*(1), e2019JE006115. https://doi.org/10.1029/2019je006115

Korablev, O., Montmessin, F., Trokhimovskiy, A., Fedorova, A. A., Shakun, A. V., Grigoriev, A. V., et al. (2018). The atmospheric chemistry suite (ACS) of three spectrometers for the ExoMars 2016 trace gas orbiter. *Space Science Reviews*, *214*(1), 7. https://doi.org/10.1007/s11214-017-0437-6

Korablev, O., Olsen, K. S., Trokhimovskiy, A., Lefèvre, F., Montmessin, F., Fedorova, A. A., et al. (2021). Transient HCl in the atmosphere of Mars. *Science Advances*, *7*(7), eabe4386. https://doi.org/10.1126/sciadv.abe4386

Krasnopolsky, V. A., Bjoraker, G. L., Mumma, M. J., & Jennings, D. E. (1997). High-resolution spectroscopy of Mars at 3.7 and 8 μm: A sensitive search for H_2O_2, H_2CO, HCl, and CH_4, and detection of HDO. *Journal of Geophysical Research*, *102*(E3), 6525–6534. https://doi.org/10.1029/96JE03766

Lefèvre, F., Trokhimovskiy, A., Fedorova, A., Baggio, L., Lacombe, G., Määttänen, A., et al. (2021). Relationship between the ozone and water vapor columns on Mars as observed by SPICAM and calculated by a Global Climate Model. *Journal of Geophysical Research*, *126*(4), e2021JE006838. https://doi.org/10.1029/2021JE006838

Liuzzi, G., Villanueva, G. L., Crismani, M. M., Smith, M. D., Mumma, M. J., Daerden, F., et al. (2020). Strong variability of martian water ice clouds during dust storms revealed from ExoMars trace gas orbiter/NOMAD. *Journal of Geophysical Research*, *125*(4). https://doi.org/10.1029/2019je006250

Liuzzi, G., Villanueva, G. L., Viscardy, S., Mège, D., Crismani, M. M. J., Aoki, S., et al. (2021). Probing the atmospheric Cl isotopic ratio on Mars: Implications for planetary evolution and atmospheric chemistry. *Geophysical Research Letters*, *48*(9). https://doi.org/10.1029/2021gl092650

LMD. (2018). The Mars climate database projects (v6.1). [Dataset]. *LMD*. Retrieved from https://www-mars.lmd.jussieu.fr/

Madeleine, J.-B., Forget, F., Millour, E., Montabone, L., & Wolff, M. J. (2011). Revisiting the radiative impact of dust on Mars using the LMD global climate model. *Journal of Geophysical Research*, *116*(E15), E11010. https://doi.org/10.1029/2011je003855

McCleese, D. J., Schofield, J. T., Taylor, F. W., Calcutt, S. B., Foote, M. C., Kass, D. M., et al. (2007). Mars Climate Sounder: An investigation of thermal and water vapor structure dust and condensate distributions in the atmosphere, and energy balance of the polar regions. *Journal of Geophysical Research*, *112*(E5), E05S06. https://doi.org/10.1029/2006je002790

Montabone, L., Forget, F., Millour, E., Wilson, R. J., Lewis, S. R., Cantor, B., et al. (2015). Eight-year climatology of dust optical depth on Mars. *Icarus*, *251*, 65–95. https://doi.org/10.1016/j.icarus.2014.12.034

Montabone, L., Spiga, A., Kass, D. M., Kleinböhl, A., Forget, F., & Millour, E. (2020). Martian year 34 column dust climatology from Mars Climate Sounder observations: Reconstructed maps and model simulations. *Journal of Geophysical Research*, *125*(8), e2019JE006111. https://doi.org/10.1029/2019je006111

NASA. (2017). NASA planetary data system node for MCS data. [Dataset]. *NASA*. Retrieved from https://atmos.nmsu.edu/data_and_services/atmospheres_data/MARS/mcs.html

Olsen, K. S., Fedorova, A. A., Kass, D. M., Kleinböhl, A., Trokhimovskiy, A., Korablev, O. I., et al. (2024a). Data from relationships between HCl, H_2O, aerosols, and temperature in the martian atmosphere: 1. Climatological outlook. [Dataset]. *Journal of Geophysical Research*, *129*. https://doi.org/10.5287/ora-qzedzvgjz

Olsen, K. S., Fedorova, A. A., Kass, D. M., Kleinböhl, A., Trokhimovskiy, A., Korablev, O. I., et al. (2024b). Relationships between HCl, H_2O, aerosols, and temperature in the martian atmosphere: 2. Quantitative correlations. *Journal of Geophysical Research*, *129*.

Olsen, K. S., Fedorova, A. A., Trokhimovskiy, A., Montmessin, F., Lefèvre, F., Korablev, O., et al. (2022). Seasonal changes in the vertical structure of ozone in the martian lower atmosphere and its relationship to water vapor. *Journal of Geophysical Research*, *127*(10), e2022JE007213. https://doi.org/10.1029/2022je007213

Olsen, K. S., Forget, F., Madeleine, J.-B., Szantai, A., Audouard, J., Geminale, A., et al. (2021). Retrieval of the water ice column and physical properties of water-ice clouds in the martian atmosphere using the OMEGA imaging spectrometer. *Icarus*, *353*, 113229. https://doi.org/10.1016/j.icarus.2019.03.006

Olsen, K. S., Lefèvre, F., Montmessin, F., Fedorova, A. A., Trokhimovskiy, A., Baggio, L., et al. (2021). The vertical structure of CO in the martian atmosphere from the ExoMars trace gas orbiter. *Nature Geoscience*, *14*(2), 67–71. https://doi.org/10.1038/s41561-020-00678-w

Olsen, K. S., Lefèvre, F., Montmessin, F., Trokhimovskiy, A., Baggio, L., Fedorova, A., et al. (2020). First detection of ozone in the mid-infrared at Mars: Implications for methane detection. *Astronomy & Astrophysics*, *639*, A141. https://doi.org/10.1051/0004-6361/202038125

Olsen, K. S., Trokhimovskiy, A., Montabone, L., Fedorova, A. A., Luginin, M., Lefèvre, F., et al. (2021). Seasonal reappearance of HCl in the atmosphere of Mars during the Mars year 35 dusty season. *Astronomy & Astrophysics*, *647*, A161. https://doi.org/10.1051/0004-6361/202140329

Pollack, J. B., Colburn, D. S., Flasar, F. M., Kahn, R., Carlston, C. E., & Pidek, D. (1979). Properties and effects of dust particles suspended in the Martian atmosphere. *Journal of Geophysical Research*, *84*(B6), 2929–2945. https://doi.org/10.1029/jb084ib06p02929

Sen, B., Toon, G. C., Blavier, J.-F., Fleming, E. L., & Jackman, C. H. (1996). Balloon-borne observations of midlatitude fluorine abundance. *Journal of Geophysical Research*, *101*(D4), 9045–9054. https://doi.org/10.1029/96JD00227

Smith, M. D. (2004). Interannual variability in TES atmospheric observations of Mars during 1999-2003. *Icarus*, *167*(1), 148–165. https://doi.org/10.1016/j.icarus.2003.09.010

Smith, M. D. (2019). THEMIS observations of the 2018 Mars global dust storm. *Journal of Geophysical Research*, *124*(11), 2929–2944. https://doi.org/10.1029/2019JE006107

Smith, M. D., Pearl, J. C., Conrath, B. J., & Christensen, P. R. (2001). One Martian year of atmospheric observations by the thermal emission spectrometer. *Geophysical Research Letters*, *28*(22), 4263–4266. https://doi.org/10.1029/2001gl013608

Trokhimovskiy, A., Fedorova, A. A., Olsen, K. S., Alday, J., Korablev, O., Montmessin, F., et al. (2021). Isotopes of chlorine from HCl in the Martian atmosphere. *Astronomy & Astrophysics*, *651*, A32. https://doi.org/10.1051/0004-6361/202140916

Trokhimovskiy, A., Perevalov, V., Korablev, O., Fedorova, A. F., Olsen, K. S., Bertaux, J.-L., et al. (2020). First observation of the magnetic dipole CO_2 main isotopologue absorption band at 3.3 μm in the atmosphere of Mars by ACS. *Astronomy & Astrophysics*, *639*, A142. https://doi.org/10.1051/0004-6361/202038134

Villanueva, G. L., Liuzzi, G., Crismani, M. M. J., Aoki, S., Vandaele, A. C., Daerden, F., et al. (2021). Water heavily fractionated as it ascends on Mars as revealed by ExoMars/NOMAD. *Science Advances*, *7*(7), eabc8843. https://doi.org/10.1126/sciadv.abc8843

Villanueva, G. L., Mumma, M. J., Novak, R. E., Radeva, Y. L., Käufl, H., Smette, A., et al. (2013). A sensitive search for organics (CH_4, CH_3OH, H_2CO, C_2H_6, C_2H_2, C_2H_4), hydroperoxyl (HO_2), nitrogen compounds (N_2O, NH_3, HCN) and chlorine species (HCl, CH_3Cl) on Mars using ground-based high-resolution infrared spectroscopy. *Icarus*, *223*(1), 11–27. https://doi.org/10.1016/j.icarus.2012.11.013

von Glasow, R., & Crutzen, P. (2003). Tropospheric halogen chemistry. In *Treatise on geochemistry* (pp. 1–67). Elsevier. https://doi.org/10.1016/b0-08-043751-6/04141-4

Wang, X., Jacob, D. J., Eastham, S. D., Sulprizio, M. P., Zhu, L., Chen, Q., et al. (2019). The role of chlorine in global tropospheric chemistry. *Atmospheric Chemistry and Physics*, *19*(6), 3981–4003. https://doi.org/10.5194/acp-19-3981-2019

Willame, Y., Vandaele, A. C., Depiesse, C., Lefèvre, F., Letocart, V., Gillotay, D., & Montmessin, F. (2017). Retrieving cloud, dust and ozone abundances in the Martian atmosphere using SPICAM/UV nadir spectra. *Planetary and Space Science*, *142*, 9–25. https://doi.org/10.1016/j.pss.2017.04.011

Wilzewski, J. S., Gordon, I. E., Kochanov, R. V., Hill, C., & Rothman, L. S. (2016). H_2, He, and CO_2 line-broadening coefficients, pressure shifts and temperature-dependence exponents for the HITRAN database. Part 1: SO_2, NH_3, HF, HCl, OCS and C_2H_2. *Journal of Quantitative Spectroscopy & Radiative Transfer*, *168*, 193–206. https://doi.org/10.1016/j.jqsrt.2015.09.003

Wong, A.-S., Atreya, S. K., & Encrenaz, T. (2003). Chemical markers of possible hot spots on Mars. *Journal of Geophysical Research*, *108*(E4), 5026. https://doi.org/10.1029/2002JE002003

Wunch, D., Toon, G. C., Blavier, J. L., Washenfelder, R. A., Notholt, J., Connor, B. J., et al. (2011). The total carbon column observing network. *Phil. Trans. R. Soc. A*, *369*(1943), 2087–2112. https://doi.org/10.1098/rsta.2010.0240

Zurek, R. W., & Smrekar, S. E. (2007). An overview of the Mars Reconnaissance Orbiter (MRO) science mission. *Journal of Geophysical Research*, *112*(E5). https://doi.org/10.1029/2006je002701